Check for updates

Femtosecond laser-structured wastepaper as a biodegradable flexible current collector for supercapacitor applications

Muhammad Qasim, [ab] Abdul Kareem, [cd] Oussama M. El-Kadri[acd] and Ali S. Alnaser [*ace]

Flexible electronics have emerged as a transformative technological trend in recent years, driven by their versatile and compelling applications in display screens, wearable sensors, and implantable medical devices. To power up these devices, considerable research efforts have been directed towards developing advanced flexible supercapacitors, owing to their potential as a reliable and efficient energy storage solution. The performance of supercapacitors is highly dependent on the design of their integral components, including the current collector, which facilitates charge transfer by connecting the active material to the external terminals. Herein, we report a high-performance, low-cost, and biodegradable flexible current collector for supercapacitors, offering a sustainable solution for energy storage applications. Wastepaper was transformed into a current collector through the incorporation of Fe^{3+} ions into the wastepaper fibers *via* chemical crosslinking and performing femtosecond laser structuring in air or inside a dilute aqueous solution of $FeCl_3$. Among the different treatments, the current collector structured in air demonstrated the highest performance. This was attributed to its superior electrical conductivity, lower charge transfer resistance, and distinct superhydrophilicity, surpassing both the unstructured counterpart and the sample structured in the $FeCl_3$ solution. Furthermore, the femtosecond laser-induced surface structures significantly contributed to improved ion diffusion and charge storage capability by increasing the electrochemically active area. The calculated areal capacitance for a sample prepared in air at 5 mV s^{-1} scan rate was 43.6 mF cm^{-2}. In addition, the current collector exhibited high areal-specific capacitance retention, which was 82% of its initial capacitance after 5000 galvanostatic charge–discharge (GCD) cycles. These results significantly outperform unstructured paper and highlight the pivotal role of laser-induced surface morphology in maximizing ion diffusion and charge storage. Our findings establish a simple yet powerful strategy for converting waste into a valuable component for sustainable energy storage applications.

1. Introduction

Population growth, coupled with the advancements in technology and the increased prevalence of digital devices and electronics, has led to a substantial surge in energy demand. It is estimated that, by 2035, the average global energy demand will reach about 778 etta joule.[1] The majority of the energy

aMaterials Science and Engineering Program, College of Arts and Science, American University of Sharjah, 26666, Sharjah, United Arab Emirates. E-mail: aalnaser@aus.edu

bDepartment of Chemical and Biological Engineering, College of Engineering, American University of Sharjah, Sharjah, 26666, United Arab Emirates

cMaterials Research Center, College of Arts and Science, American University of Sharjah, 26666, Sharjah, United Arab Emirates

dDepartment of Biology, Chemistry, and Environmental Sciences, College of Arts and Science, American University of Sharjah, PO Box 26666, Sharjah, United Arab Emirates

eDepartment of Physics, College of Arts and Sciences, American University of Sharjah, 26666, Sharjah, United Arab Emirates

supply is derived from conventional energy sources, such as fossil fuels, which contribute to significant challenges, including pollution, climate change, and public health issues.[2] While renewable sources, such as solar and wind energy, are viable alternatives, their inherent intermittency presents a challenge, with performance fluctuating depending on the time of day, season, and other unpredictable factors.[3] This leads to periods where the energy supply becomes either insufficient or in excess compared to the demand. To address this issue, energy storage devices (ESDs) play a critical role in storing the excess energy during peak production periods and supplying the saved energy during downtime.[4] Among the available ESDs, supercapacitors have attracted significant interest as next-generation devices owing to their rapid charge and discharge characteristics, high performance, enhanced safety, prolonged service life, high power and energy density, and cyclic stability.[1,5,6] These characteristics also make supercapacitors highly suitable for use in flexible and wearable electronic

devices, such as health monitors, flexible displays, and foldable screens, that have become a prominent technological trend in recent years.[7,8]

In general, the electrochemical performance of a super-capacitor depends largely on the material of its components. The principal components include the active electrode material, that serves as the charge storage medium, the electrolyte/membrane that allows for charge conduction, and the current collector that transfers the current from the external source during charging and delivers the stored energy during operation.[1,6] Among these components, the current collector plays a crucial role in connecting the supercapacitor's active material to the external terminals, ensuring efficient charge transfer.[9] An ideal current collector must exhibit high electrical conductivity, low contact resistance and strong adhesion with the active material, high specific surface area, low weight and cost, excellent mechanical, electrochemical, and thermal stability, and high flexibility in case of flexible supercapacitors.[10] Extensive research efforts have been dedicated to developing and utilizing highly efficient current collectors in flexible super-capacitors, given their indispensable role in establishing strong electrical contact between the active material and the external terminals.

In this context, carbon, polymer, and metal-based flexible current collectors have been proposed. For example, Notarianni et al.[11] employed carbon nanotube (CNT) film as a current collector in a graphene-based flexible supercapacitor. It was reported that the conductive CNT film was not only equivalent to gold as a current collector but also formed a very strong bond with the graphene film. The resulting electrode exhibited a capacitance of $\sim$4.3 mF cm^{-2} and an energy density in the range 8–14 Wh kg^{-1}. Shulga et al.[12] prepared flexible current collectors based on graphene oxide (GO) and poly-tetrafluoroethylene (PTFE) films. The specific capacitance in this case exceeded 130 F g^{-1} and remained stable over prolonged cycling. Hepowit et al.[13] proposed flexible polymer/carbon-based current collector sheets consisting of acrylonitrile–butadiene rubber (NBR) and vapor-grown carbon fiber (VGCF). When used with polypyrrole (PPy) active material, the PPy/VGCF/NBR composite electrode with 30 wt% VGCF achieved a maximum specific capacitance of 125.8 F g^{-1}. Ren et al.[14] prepared a flexible current collector by electrodepositing Ni on laser-drilled stainless-steel sheets filled with epoxy resin. In this case, MnO$_2$ was employed as the active material. The maximum specific capacitance in this case reached 2.4 F cm^{-2}. Also, a high cyclic stability was observed with a capacitance retention of 90% after 5000 charge/discharge cycles at a current density of 31.8 mA cm^{-2}. While these flexible current collectors show great promise, their commercial implementation is hindered by challenges such as high material costs, tedious synthesis procedures, and limited environmental sustainability. As such, there is a pressing need to develop flexible current collectors and electrodes for supercapacitors that are inexpensive, easy to synthesize, lightweight, sustainable, and environmentally friendly.

One promising approach to develop flexible supercapacitors is to exploit waste materials, such as paper, by repurposing

them for sustainable and cost-effective fabrication of flexible current collectors. Wastepaper offers several distinct advantages, including very high flexibility and bendability, light-weight, low cost, and porous structure for active material deposition. Also, it is abundantly available, with approximately 400 million tons of wastepaper generated annually.[15] In addition, the inherent biodegradability of wastepaper makes it an ideal candidate for advancing sustainable energy storage. However, to utilize the inherently insulating wastepaper as a current collector, modifications are necessary to incorporate suitable electrically conductive materials into the matrix.[16] There have been attempts to modify paper to make it suitable as a current collector for supercapacitors. For example, Yuan et al.[17] prepared flexible and high-performing electrodes by depositing a thin film of Au on printing paper using an e-beam evaporation system, followed by electrochemical growth of polyaniline (PANI) nanowires via oxidation of aniline in a three-electrode system. The resulting supercapacitor exhibited an energy density of $\sim$0.01 Wh cm^{-3} and a power density of $\sim$3 W cm^{-3}. Despite the promising results, the fabrication process was relatively sophisticated. Li et al.[18] prepared flexible electrodes using bacterial cellulose (BC), multiwalled carbon nanotubes (MWCNTs), and PANI. First, BC paper was synthesized from its suspension via vacuum filtration. Next, MWCNTs ink solution was poured onto the paper to form BC-MWCNTs paper. In the final step, electrochemical polymerization was employed to coat PANI on top of BC-MWCNTs paper. The resulting BC-MWCNTs-PANI electrode was flexible and exhibited a specific capacitance of 656 F g^{-1} at a current density of 1 A g^{-1}. Again, the fabrication procedure was relatively tedious, and the high cost of MWCNTs presented an additional challenge. Li et al.[19] employed an electroless deposition method to prepare flexible current collectors consisting of metallic Ni layer, composed of spiny Ni nanospheres of 400 nm diameter, on top of a filter paper. When used with MnO$_2$ active material, the areal specific capacitance was found to be 1095 mF cm^{-2} at 1 mA cm^{-2}. The electrochemical performance was attributed to the high contact area provided by the hierarchical porous fiber structure of the paper and the low contact resistance between the active material and the current collector. However, the deposition method in this case involved the use of complex and harsh chemicals, such as chloroplatinic acid and hydrazine.

Herein, we demonstrate that wastepaper can be transformed into an efficient, low-cost, lightweight, and biodegradable current collector for flexible supercapacitors. A two-step strategy was employed for this purpose. First, wastepaper underwent femtosecond laser surface structuring for enhancing the electrochemical surface area. The femtosecond laser structuring step was performed in air or inside a dilute aqueous solution of FeCl$_3$ to systematically study the effect of processing environment on the laser-induced surface structures and the electrochemical performance of the resulting current collectors. After the laser structuring step, the sample was allowed to chemically crosslink in FeCl$_3$ aqueous solution for conductivity enhancement by embedding Fe^{3+} ions into the paper fibers. The incorporation of Fe^{3+} ions occurred via coordination bonds with the surface polar groups, such as hydroxyl (–OH), carbonyl (C=

O), and carboxyl (–COOH) groups. $FeCl_3$ was selected for chemical crosslinking due to its low cost and ease of availability. Although zirconyl(IV) chloride ($ZrOCl_2$) has been reported as an effective crosslinking agent for wastepaper fibers, its higher cost, limited availability, and additional safety considerations make $FeCl_3$ a more practical and scalable choice.[20,21] The electrochemical measurements were performed to probe the intrinsic capacitive response and interfacial charge-transfer characteristics of the wastepaper-based current collector. The electrochemical performance of the prepared current collectors was assessed using 1 M KOH electrolyte solution. For the current collector prepared by laser structuring in air, the calculated areal capacitance at a 5 mV s^{-1} scan rate was 43.6 mF cm^{-2}, while 82% of the initial areal specific capacitance was retained after 5000 GCD cycles. This current collector outperformed those prepared without femtosecond laser structuring and those processed inside the $FeCl_3$ solution, due to its unique surface structures and superhydrophilic character. The proposed methodology not only enables the fabrication of high-performing current collectors for flexible supercapacitors but also offers the added advantages of waste upcycling and reducing the environmental impacts associated with wastepaper disposal. Furthermore, the presented approach provides a sustainable and eco-friendly route for fabricating efficient current collectors by utilizing reagent-free femtosecond laser processing and a very dilute $FeCl_3$ solution. The main contribution of this work is demonstrating the substrate's conductivity, superhydrophilicity, mechanical robustness, and long-term stability, which are the key current-collector-specific advantages.

2. Experimental

2.1. Materials

Wastepaper was collected from offices at the American University of Sharjah, University City, Sharjah, United Arab Emirates. The offices utilized A4 printing paper (basis weight: 80 g m^{-2}, Universal, NAVIGATOR Office Paper Solutions, Portugal). Ferric chloride hexahydrate ($FeCl_3 \cdot 6H_2O$, purity: ≥99%) was procured from VWR International GmbH, Germany. For electrochemical studies, analytical grade potassium hydroxide (KOH, ACS reagent, assay: ≥85%) was used as an electrolyte and was procured from Sigma Aldrich, USA. All chemicals were used as received, without additional purification.

2.2. Current collector preparation

Wastepaper was first cut into a sample of appropriate size. The sample subsequently underwent femtosecond laser structuring in air under ambient conditions. A fiber-based femtosecond (fs) laser (AFSUFFL-300-2000-1030-300, Active Fiber Systems GmbH, Jena, Germany) was employed for this purpose. The laser source generated Gaussian pulses with a central wavelength of 1030 nm. The maximum power, pulse duration, and repetition rate were 300 W, 50 fs, and 50 kHz, respectively. A half-wave plate and a thin-film polarizer (Thorlabs Inc., USA) were used to attenuate and control the laser beam power. A Maestro

galvanometric scan head (FARO, USA) fitted with a focusing f-theta lens was used to raster scan the laser beam on the sample. During laser structuring, an average power of 3 W was utilized while the line spacing and scanning speed were set at 200 μm and 200 mm s^{-1}, respectively. The focal spot size on top of the sample surface was ~50 μm. The laser beam was raster scanned over the sample only once and in a crosshatch configuration. Following laser structuring in air, the sample was subjected to chemical crosslinking for 4 hours in an aqueous solution of $FeCl_3$ (concentration: 50 mM) to embed Fe^{3+} ions into the chemical structure of the wastepaper fibers. The volume of $FeCl_3$ solution utilized was 0.5 mL per cm^2 of the wastepaper. After crosslinking, the sample was thoroughly rinsed with deionized water to remove any excess ions. In the final step, the sample was dried for 2 hours in a laboratory drying oven at 70 °C. The dried sample was then employed as a current collector. This current collector, which was laser structured in air, was designated as LS-air, where LS denoted laser structuring. Using a similar methodology, another current collector was prepared by performing femtosecond laser structuring while the sample was immersed in a dilute aqueous solution of $FeCl_3$. Specifically, the sample was placed in a Petri dish and a 50 mM aqueous $FeCl_3$ solution was added until the liquid level was approximately 2 mm above the surface of the sample. Subsequently, laser structuring was carried out on the immersed sample. After laser structuring, the sample was subjected to chemical crosslinking for 4 hours in a 50 mM aqueous solution of $FeCl_3$, followed by drying for 2 hours in a laboratory drying oven at 70 °C. This current collector sample was named LS-solution. Additionally, a third current collector was prepared through chemical crosslinking alone, without laser structuring, using the same $FeCl_3$ solution, crosslinking time, and drying conditions. This sample was designated as US, indicating an unstructured sample. Fig. 1 shows the schematic diagram of femtosecond laser structuring system employed in this study.

2.3. Characterizations

The morphology of the prepared current collectors was investigated using a scanning electron microscope (SEM, VEGA 3 LMU, TESCAN, Czech Republic). All samples were sputter-coated with Au/Pd before imaging. An energy dispersive X-ray spectroscopy (EDX, INCAx-act, Oxford Instruments) detector fitted within the SEM was used for elemental and compositional analysis. Fourier transform infrared spectroscopy (FTIR) analysis was performed using an FTIR spectroscope (IRSpirit, Shimadzu, Kyoto, Japan) in attenuated total reflectance mode (ATR-FTIR). Water contact angles were measured at ambient conditions using a drop shape analyzer (DSA100M, Kruss GmbH, Germany). All contact angle measurements were conducted using a 5 μL deionized water droplet. Chemical analysis was performed using X-ray photoelectron spectroscopy (XPS). For this, ESCALAB QXi XPS system (Thermo Fisher Scientific Inc., Waltham, MA, USA) was employed. All XPS analyses were carried out with Al Kα X-rays ($h\nu = 1486.6$ eV). Survey spectra were acquired at an energy resolution of 1.0 eV over 25 scans, while high-resolution spectra were collected at 0.1 eV resolution
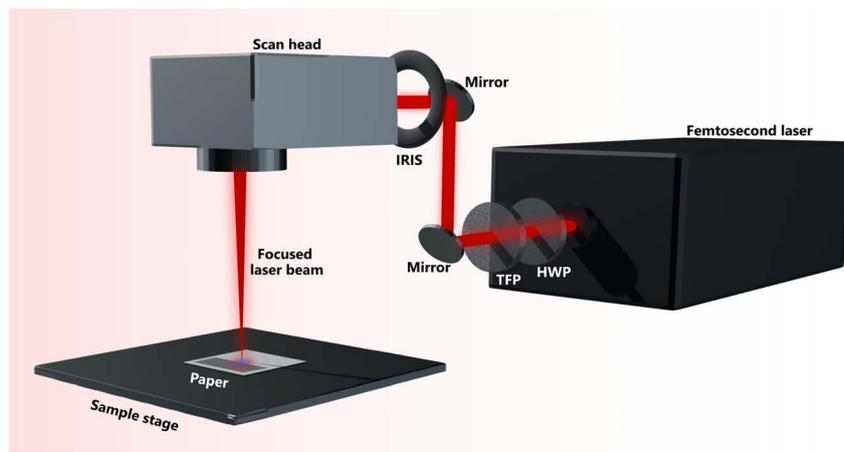
Fig. 1 Femtosecond laser structuring system for preparing current collectors from wastepaper. TFP: thin-film polarizer, HWP: half-wave plate.

over 50 scans. XPSPEAK41 software was employed for spectral deconvolution of the high-resolution spectra by applying Gaussian–Lorentzian peak fitting.

2.4. Electrochemical analysis

All electrochemical investigations were conducted using the CHI 660E electrochemical workstation (CH Instruments Inc., Austin, Texas, USA). Tests were performed using a three-electrode setup containing 1 M KOH electrolyte solution. The current collector derived from wastepaper was used as the working electrode (1×1 cm^2) (photos of the current collectors are depicted in Fig. S1), while Pt and Hg/HgO served as the counter and reference electrodes, respectively. In case of cyclic voltammetry (CV) analysis, the areal capacitance (C_{sp}) in mF cm^{-2} was determined as follows:[22]

$$C_{sp} = \frac{\int I dV}{2sA\Delta V} \qquad (1)$$

where, $\int I dV$ represents the area under the CV curve, s is the scan rate (V s^{-1}), ΔV is the potential window (V), and A is the active area of the studied working electrode (cm^2).

In case of galvanostatic charge–discharge (GCD) analysis, the following equation was used to calculate the areal-specific capacitance:[23]

$$C_{sp} = \frac{I\Delta t}{A\Delta V} \qquad (2)$$

where, I is the applied current (mA) and Δt is the discharge time (s).

3. Results and discussion

3.1. Surface morphology

The SEM images, along with the corresponding elemental mapping and elemental compositions, of the three current collectors prepared in this study are presented in Fig. 2 and S2–S4 SI. The US current collector exhibited a morphology similar to that of typical paper. A micro-fibrous structure was observed, in which cellulose fibers of varying shapes and sizes

were intertwined in a complex, interconnected, web-like network. EDX analysis confirmed the incorporation of Fe^{3+} ions into the fibers of the US current collector, with the sample exhibiting an Fe content of 15.4 wt%. This indicated successful crosslinking of the sample with Fe^{3+} ions. The crosslinking mechanism involved formation of coordination bonds between Fe^{3+} ions and the polar functional groups in the cellulose and hemicellulose fibers of the wastepaper. Wastepaper fibers are known to contain hairy nanofibrils that are rich in polar functional groups, such as hydroxyl (–OH), carbonyl (C=O), and carboxyl (–COOH) groups.[21,24] Upon crosslinking, coordination bonds were formed between the Fe^{3+} ions and these polar functional groups present on the nanofibrils.[21] This process resulted in the incorporation of Fe^{3+} ions into the US current collector.

For the LS-solution current collector, prepared by laser structuring inside FeCl$_3$ solution, square-shaped patterns were introduced on the surface. These patterns, appearing as vertical and horizontal lines, were formed due to the ablation effects induced by the femtosecond laser beam. The deposition of laser energy onto the wastepaper sample led to surface ablation, resulting in the ejection of material and formation of well-defined, square-shaped surface patterns. The laser-induced surface patterns were important for the electrochemical performance of the LS-solution current collector. The square-shaped surface features substantially increased the surface area, offering more active sites for the electrochemical reactions to occur. The Fe content for the LS-solution current collector was also slightly higher (18.4 wt%) compared to the US current collector. This can be attributed to the increased surface area resulting from laser structuring, which exposed a greater number of polar functional groups, thereby facilitating increased crosslinking with the Fe^{3+} ions.

In this study, laser-induced surface patterns were found to play a critical role in enhancing the electrochemical performance of the current collectors. These surface patterns resulted directly from the interactions between the femtosecond laser beam and the wastepaper substrate. For nonmetallic materials with a low free electron density, such as wastepaper, the
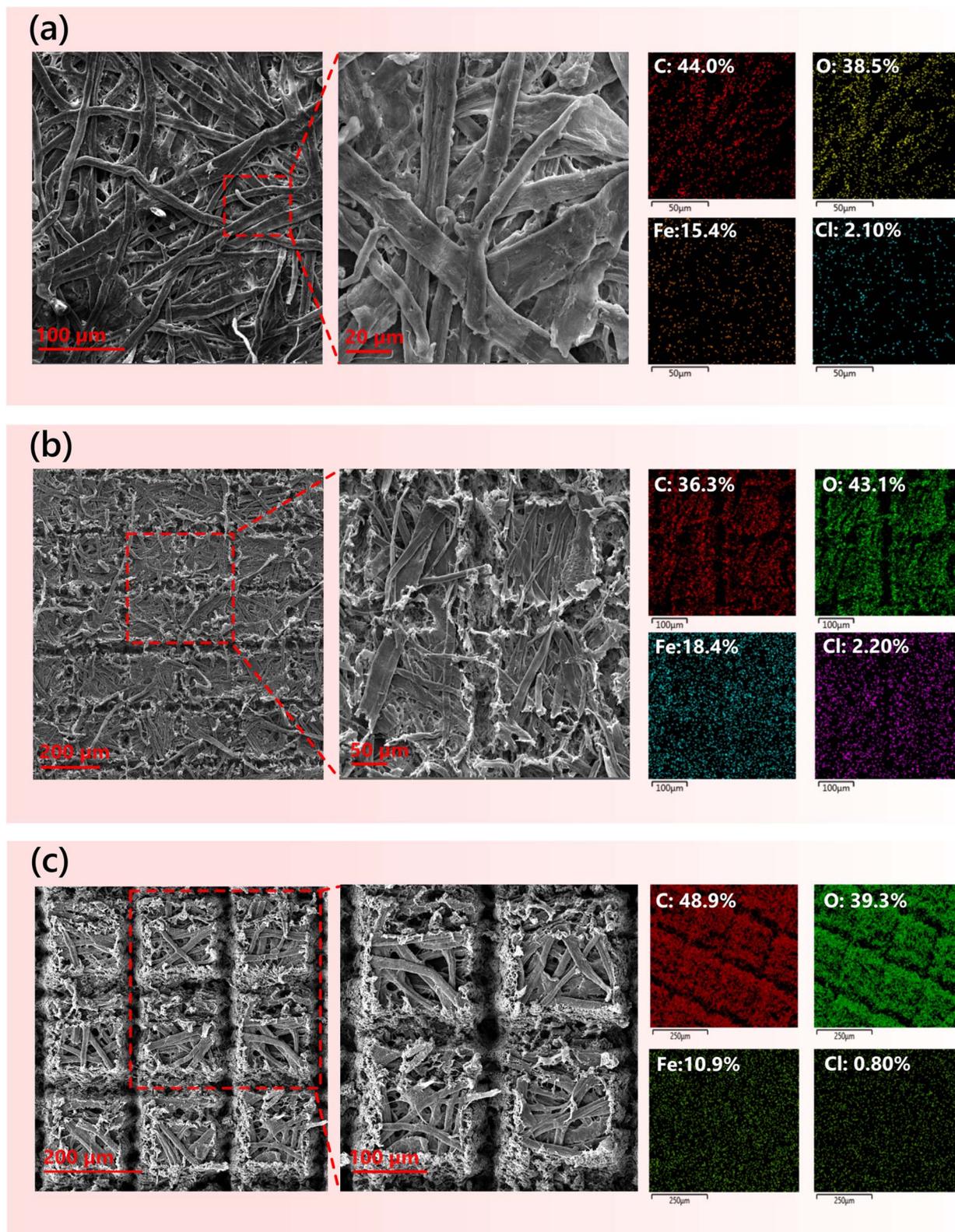
Fig. 2 SEM images and EDX elemental layered images of (a) US (b) LS-solution and (c) LS-air current collectors.

femtosecond laser ablation mechanism primarily proceeds in two distinct stages. In the first stage, free electrons are generated through ionization. This process involves both photoionization and impact ionization mechanisms. In case of photoionization, free electrons are generated by two sub-processes, namely, tunnel ionization and multiphoton

ionization. Tunnel ionization is induced by the super-strong electromagnetic field generated during the interaction between the femtosecond laser and the non-metallic substrate. This intense field lowers the Coulomb potential barrier for the valence band electrons, allowing them to pass through the barrier *via* tunneling effect and transition into the conduction band, thereby becoming free electrons. Multiphoton ionization, on the other hand, involves absorption of multiple photon energies by the valence band electrons. This provides sufficient energy for their excitation into the conduction band, allowing them to become free electrons. Additionally, free electrons are generated *via* impact ionization, a mechanism that is also referred to as avalanche ionization. In this mechanism, free electrons generated during photoionization are used as seed electrons. Once the low-energy free electrons absorb more than one photon and transition to a high-energy state in the conduction band, the free electrons obtain higher levels of kinetic energy. Upon colliding with other valence electrons, energy transfer takes place, which results in the generation of two low-energy free electrons. These low-energy free electrons subsequently repeat the process by absorbing photons, colliding, and finally ionizing again to create a chain reaction that continues to generate free electrons. In the second stage of ablation, a phase change occurs which is primarily driven by the interaction of the free electrons with the lattice. Following ionization and electron heating, a sufficiently large number of free electrons accumulate inside the substrate, imparting a transient metallic behavior to the originally non-metallic substrate. The phase change primarily occurs due to impulsive Coulomb explosion, involving a dense, high-pressure plasma. Due to the spatial confinement of the plasma in a limited region and continuous absorption of the laser energy, the plasma attains extremely high pressures and temperatures. Consequently, the plasma undergoes a rapid and instantaneous expansion and eventually bursts outward, leading to the ejection of ionized material from the substrate. This ejection of ablated material results in the formation of surface microstructures and causes permanent damage to the substrate, as observed in the case of LS-solution current collector.[25–27]

In case of the LS-air current collector, laser structuring in ambient air led to the formation of more pronounced surface patterns with significantly deeper surface channels compared to the LS-solution current collector. This difference can be attributed to the more intense ablation in ambient air induced by the femtosecond laser beam. In other words, the laser fluence at the sample surface in air was higher compared to that during laser structuring on the immersed sample. In the case of the LS-solution sample, the focused laser beam induced bubble generation due to localized water evaporation. The formation, growth, and subsequent collapse of these bubbles at the laser-liquid interface attenuated the laser beam through introduction of scattering and refraction effects. As a result, the effective laser fluence reaching the sample surface reduced. Additionally, the $FeCl_3$ solution further disturbed the optical pathway of the laser beam through absorption and refractive index variations. These effects caused the laser beam to diffuse and become partially defocused, which further resulted in a lower fluence at

the sample surface.[28–31] Taken together, the lower fluence during laser structuring in $FeCl_3$ solution resulted in shallower ablation features and less pronounced structural features on the LS-solution current collector. On the other hand, laser structuring in air involved direct delivery of the laser energy to the sample surface, without any attenuation effects, which produced higher fluence at the sample surface and promoted more efficient material removal and more intense ablation in case of LS-air current collector. The intense ablation, in turn, exposed a significantly higher number of polar functional groups on the surface of LS-air current collector. However, with the given Fe^{3+} concentration and crosslinking duration, not all the exposed functional groups could be successfully crosslinked. As a result, the Fe content on the LS-air current collector was lower (10.9 wt%) compared to the LS-solution current collector.

3.2. Surface chemistry analysis

Surface chemical analysis was conducted using FTIR spectroscopy to verify the crosslinking process and the incorporation of Fe^{3+} ions into the chemical matrix of the wastepaper current collectors. The FTIR spectra of wastepaper and US, LS-solution and LS-air current collectors are presented in Fig. 3. All FTIR spectra exhibited the characteristic peaks associated with cellulose. These peaks appearing around 1371, 1207, 1161, 1100, and 900 cm^{-1} corresponded to the C–H bending, O–H deformation, C–O–C asymmetric vibration, glucose ring stretch (asymmetric), and glucose ring stretching, respectively.[32,33] In addition, all samples displayed the characteristic peaks of hemicellulose around 2926, 1745, 1309 and 1026 cm^{-1}. These corresponded to asymmetrical CH_2 stretching, C=O stretching in O=C–OH group, C–H vibration band, and C–O stretching, respectively.[21,34,35] The observation of these bands indicated that all the samples were primarily composed of cellulose and hemicellulose. Upon crosslinking, specific changes were
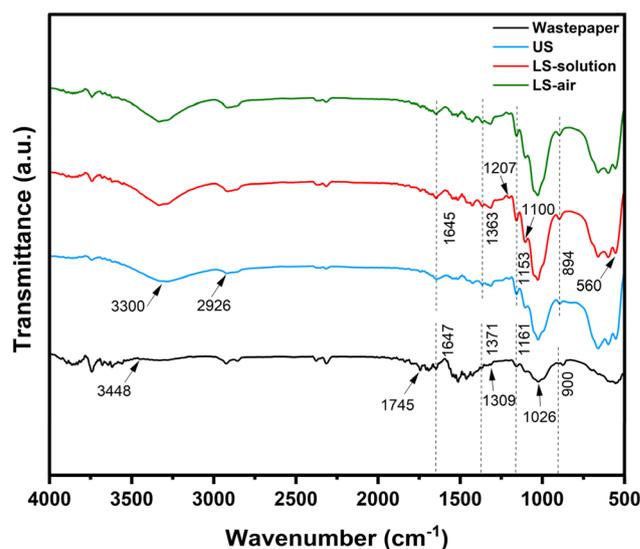

Fig. 3 FTIR spectra for pristine wastepaper and US, LS-solution, and LS-air current collectors.

observed in the FTIR spectra of the US, LS-solution, and LS-air samples. The chemical crosslinking induced by Fe^{3+} ions was confirmed by distinct changes in the FTIR spectra involving the appearance of a new band for Fe–O bond, shifts and intensity changes in the bands associated with cellulose and hemicellulose, and changes in the O–H stretching vibration region. Unlike the wastepaper sample, the US, LS-solution and LS-air samples displayed a characteristic band appearing at 560 cm^{-1}. This band, absent in wastepaper sample, corresponded to the Fe–O stretch band and confirmed the successful incorporation of Fe^{3+} ions *via* chemical crosslinking that occurred within the chemical structure of the US, LS-solution, and LS-air samples.[36] In addition, the FTIR spectra showed that the C–H bending in the cellulose fraction of the US, LS-solution, and LS-air samples shifted to lower wavenumber, from 1371 to ∼1363 cm^{-1}. Also, the –O– stretching vibrations in the cellulose shifted from 1161 to 1153 cm^{-1}. These results indicated Fe^{3+} ion-induced chemical crosslinking, changes in the cellulose molecular environment, and coordination of the Fe^{3+} ions with the ring oxygens and –OH groups of the cellulose.[21,37] Similarly, in case of the hemicellulose fraction, the glycosidic C–O stretching (900 cm^{-1}) in the pristine wastepaper shifted to lower wavenumbers in the US, LS-solution, LS-air samples (∼894 cm^{-1}). This again indicated successful coordination of the Fe^{3+} ions with the ring oxygens and –OH groups of the hemicellulose fraction in the paper fibers.[21] Additionally, chemical crosslinking was confirmed by changes in the

hemicellulose-related peak at 1745 cm^{-1}. This peak, related to C=O stretching in the O=C–OH group, showed a reduction in intensity for the US, LS-solution, and LS-air samples, indicating that the Fe^{3+} ions coordinated with the C=O group oxygen atoms.[21] Also, the peak at 3448 and 1647 cm^{-1} in pristine wastepaper was attributed to the hydroxyl groups and water present on the surface of cellulose fibers. Upon crosslinking, these peaks shifted to 3330 and 1645 cm^{-1}, suggesting the modification of the chemical structure due to chemical crosslinking and incorporation of Fe^{3+} ions.[38] In addition, the stretching vibration of O–H, appearing around 3330 cm^{-1}, became more intense and broader for the US, LS-solution, and LS-air samples. This indicated that, for these samples, the O–H bond weakened because of its coordination with the Fe^{3+} ions during the crosslinking reaction.[39] The wastepaper sample, on the other hand, showed a narrow, less intense O–H band around 3448 cm^{-1}. The appearance of this band at a higher wavenumber along with its narrow shape indicated the presence of uncoordinated and isolated O–H groups, highlighting the absence of crosslinking.[40] Overall, the FTIR spectra of the US, LS-solution, and LS-air samples indicated successful coordination and chemical crosslinking of Fe^{3+} ions within the cellulose and hemicellulose fractions of the paper fibers.

To further confirm the crosslinking of Fe^{3+} ions within the chemical matrix of the wastepaper current collectors, XPS analysis was conducted. Fig. 4 presents the XPS survey spectrum for the US, LS-solution and LS-air current collectors. The survey
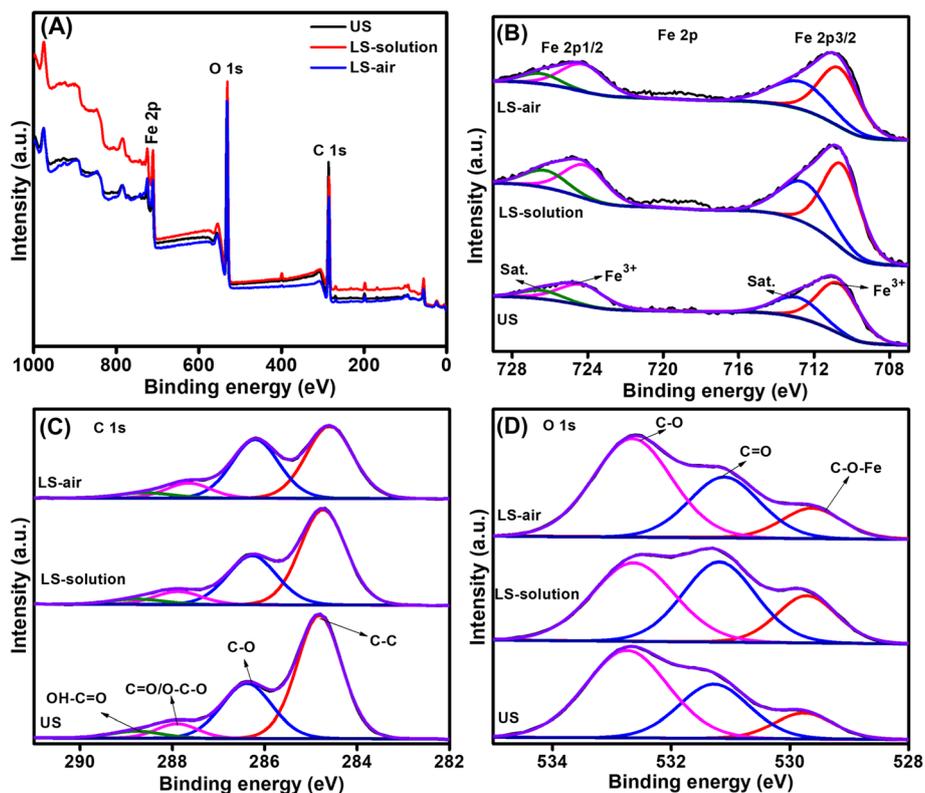

Fig. 4 XPS spectra for the US, LS-solution, and LS-air current collectors: (A) survey spectra, and high-resolution spectra for (B) Fe 2p, (C) C 1s, and (D) O 1s.

spectrum revealed characteristic peaks for C 1s and O 1s, consistent with the cellulose and hemicellulose composition of the wastepaper fibers. In addition, the XPS spectrum displayed a peak for Fe 2p, indicating that Fe^{3+} ions were successfully incorporated into the chemical structure of all the current collectors. Fig. 4(B) shows the core level spectra of Fe 2p of all three current collectors, where two pairs of peaks were observed at 710.9 and 724.5 eV corresponding to Fe $2p_{3/2}$ and Fe $2p_{1/2}$, confirming the +3 oxidation state of Fe. The peaks observed at 713.0 and 726.4 eV are attributed to satellite peaks. Similar peaks were observed for all three current collectors, which confirmed the presence of Fe^{3+} in all the current collectors. Furthermore, the deconvoluted spectra of C 1s showed four peaks at 284.8, 286.4, 287.9 and 288.7 eV, ascribed to C–C, C–O, C=O/O–C–O and OH–C=O. A shift towards lower binding energy was observed in the LS-solution and LS-air sample, which could be due to the laser structuring (Fig. 4(C)). To gain a deeper understanding of the chemical interactions, the high-resolution O 1s spectrum was deconvoluted, as shown in Fig. 4(D). Upon deconvolution, the high-resolution spectrum of O 1s in LS-air current collector revealed three distinct peaks. These peaks around 529.5, 531.6, and 532.8 eV corresponded to Fe–O–C, C–O, and C=O groups, respectively.[21] While the C–O and C=O corresponded to the hydroxyl and carbonyl groups in cellulose and hemicellulose, the presence of peak Fe–O–C indicated that Fe^{3+} ions formed coordination bonds with these oxygen-containing functional groups in the LS-air current collector. Similar features were observed in the US and LS-solution current collectors, where the presence of Fe 2p and

Fe–O–C peaks in the survey and high-resolution O 1s spectra confirmed the incorporation and chemical crosslinking of Fe^{3+} ions in these samples as well. Overall, the XPS results, in conjunction with the FTIR analysis, strongly suggested chemical integration of Fe^{3+} ions into the wastepaper current collectors, wherein stable bonds were formed with the oxygen atoms in the cellulose and hemicellulose fractions.

3.3. Electrochemical analysis

The electrochemical performance of the prepared wastepaper-based current collectors was evaluated using CV, GCD and electrochemical impedance spectroscopy (EIS) analysis in 1 M KOH electrolyte. The results revealed clear differences among the three processing methods. The CV curves for the three current collectors are shown in Fig. 5. In all cases, the CV curves exhibited quasi-rectangular shapes, indicative of electric double-layer capacitance (EDLC) behavior in the prepared samples. This suggested that energy storage occurred through the electrostatic accumulation of ions at the interface between the current collector and the electrolyte, forming an electric double layer.[41] For the sample that was only crosslinked for 4 hours in $FeCl_3$ solution without laser treatment (US sample), the CV curves demonstrated the weakest current responses across all scan rates (Fig. 5(A)). This is attributed to the smooth and non-porous surface, as confirmed by the SEM images (Fig. 2(a)), which showed a lack of structural modifications or increased surface area in case of the US sample. Additionally, compared to the pristine wastepaper, the crosslinking process increased the
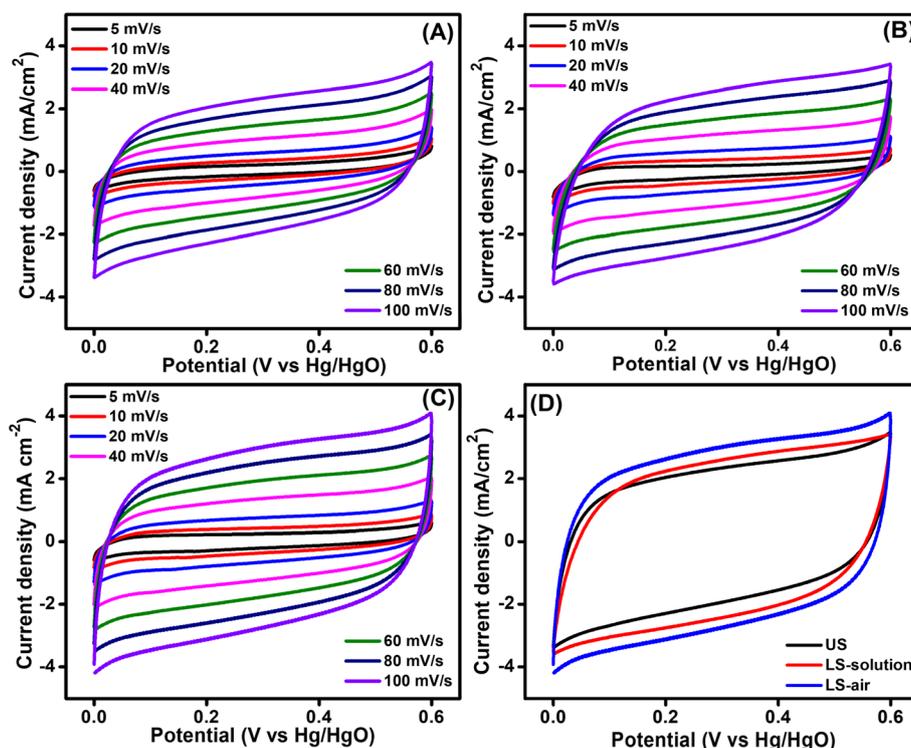

Fig. 5 CV curves of (A) US, (B) LS-solution, (C) LS-air current collectors at different scan rates from 5 to 100 mV s^{-1} and (D) comparative CV curves at 100 mV s^{-1} scan rate for all the samples in 1 M KOH.

hydrophobicity of the US current collector, as evidenced by a water contact angle (WCA) of 128.6° (SI Fig. S5). This enhancement in hydrophobicity upon crosslinking is attributed to the coordination of Fe^{3+} ions with the surface polar groups, such as hydroxyl (–OH), carbonyl (C=O), and carboxyl (–COOH) groups. These interactions promoted the self-assembly of cellulose nanofibrils in the wastepaper, resulting in formation of compact structures with fewer –OH groups available for water sorption.[21] Consequently, the reduced number of polar groups minimized interactions with water and the electrolyte, thereby imparting a hydrophobic character to the US current collector. The hydrophobic character in turn decreased the electrode–electrolyte interface interaction, resulting in weak current responses during CV.

In contrast, the sample treated with laser structuring in the $FeCl_3$ solution (LS-solution sample) exhibited better electrochemical performance compared to the US current collector. The CV curves for this sample showed significantly higher current responses (Fig. 5(B)), indicating enhanced charge storage and transfer capabilities. This can be attributed to the patterned, rough surface created by the laser treatment, as shown in the SEM images in Fig. 2(b). The formation of square-shaped arrays *via* laser ablation increased the electrochemically active surface area, thereby facilitating improved ion diffusion compared to the US current collector. Additionally, the Fe content for the LS-solution current collector was 18.4 wt%, which was higher compared to that for the US current collector. This resulted in enhanced current responses for the LS-solution sample, owing to higher conductivity from the greater incorporation of Fe^{3+} ions within its structure. The increase in Fe content is attributed to the larger surface area generated by femtosecond laser structuring, which exposed a larger number of polar functional groups on the surface and made them available for crosslinking with the Fe^{3+} ions. Additionally, the ablation zones facilitated deeper penetration of Fe^{3+} ions during the crosslinking process, further increasing the likelihood of crosslinking with the surface polar groups. Together, the higher Fe content on the LS-solution sample and the increased electrochemically active area contributed to the enhanced electrochemical performance of the LS-solution current collector.

The LS-air sample, which underwent femtosecond laser structuring in air followed by 4 hours of crosslinking in $FeCl_3$ solution, exhibited the best electrochemical performance among all samples. The CV curves for this sample demonstrated better current responses compared to the US and LS-solution samples (Fig. 5(C)). The SEM images in Fig. 2(c) revealed a grid-like structured surface with very deep laser ablated zones, which could increase the electrochemical surface area. Furthermore, contact angle measurements (SI Fig. S5) confirmed the superhydrophilic nature of the LS-air current collector, characterized by a WCA of 0° and rapid droplet spreading upon surface contact (SI Video 1). The superhydrophilic nature of the LS-air current collector likely enhanced the electrode–electrolyte interface interaction, facilitating more efficient ion transport and charge transfer during electrochemical measurements. The superhydrophilicity of the

LS-air sample was attributed to the deep laser ablation zones created during laser structuring in air. The deep ablation zones exposed a significantly larger number of polar functional groups. However, not all these groups were crosslinked with Fe^{3+} ions within the given crosslinking time and the concentration of the employed $FeCl_3$ aqueous solution. Consequently, the Fe content on the LS-air sample was the lowest (only 10.9 wt%). Despite this lower Fe loading, the electrochemical performance of the LS-air sample was better compared to the LS-solution sample. Although the LS-solution sample exhibited a higher Fe content, an inferior performance compared to the LS-air sample was observed due to its significantly lower hydrophilicity. The LS-solution sample was able to achieve more extensive crosslinking after laser structuring due to lower number of exposed surface polar groups compared to the LS-air sample. The WCA of LS-solution sample was in fact 154.5° (SI Fig. S5), which likely hindered electrolyte penetration during electrochemical measurements. Thus, the LS-air sample achieved the best electrochemical performance due to the synergistic effect of a highly structured surface that maximized the electrochemically active surface area and a superhydrophilic character that promoted efficient interaction with the electrolyte.

The areal capacitance values for the fabricated current collectors are provided in Table 1. Also, the areal capacitance calculated using CV curves at different scan rates are compared in Fig. S6(a). At a 5 mV s^{-1} scan rate, the sample treated with laser structuring in air exhibited the highest areal capacitance value of 43.6 mF cm^{-2}. For better understanding, the CV cycles were compared at a scan rate of 100 mV s^{-1} for all three samples in Fig. 5(D). This sample achieved the highest current responses, followed by the LS-solution sample, while the US sample showed the weakest performance. As can be observed from Fig. 5(D), a higher capacitive current response was observed for the LS-air sample compared to LS-solution and US sample. Usually, a larger capacitive (non-faradaic) current response in the CV curves indicates higher double-layer capacitance (C_{dl}), which correlates with increased electrochemically active surface area (ECSA). The enhanced performance of the LS-air sample can be attributed to its increased hydrophilic nature, which improved both ion accessibility and the electrode–electrolyte interface reaction. On the other hand, the limited low hydrophilicity of the US sample restricted the electrode to electrolyte interface reaction, making it the least effective current collector.

Further, we performed GCD testing of the three samples under various current densities for further detailed electrochemical study. For all samples, the GCD curves exhibited a nearly linear discharge slope with ideal triangular shapes. This further confirmed the EDLC behavior of these samples.[42] The sample processed without laser treatment, referred to as US sample, showed the shortest charge–discharge times across all current densities (Fig. 6(A)), indicating poor energy storage capability. This performance was closely tied to its surface morphology, as observed in the SEM images, which revealed a smooth surface with limited electrochemical surface area and activity. The LS-solution sample exhibited improved

Table 1 Comparison of areal capacitance from CV and areal-specific capacitance from GCD

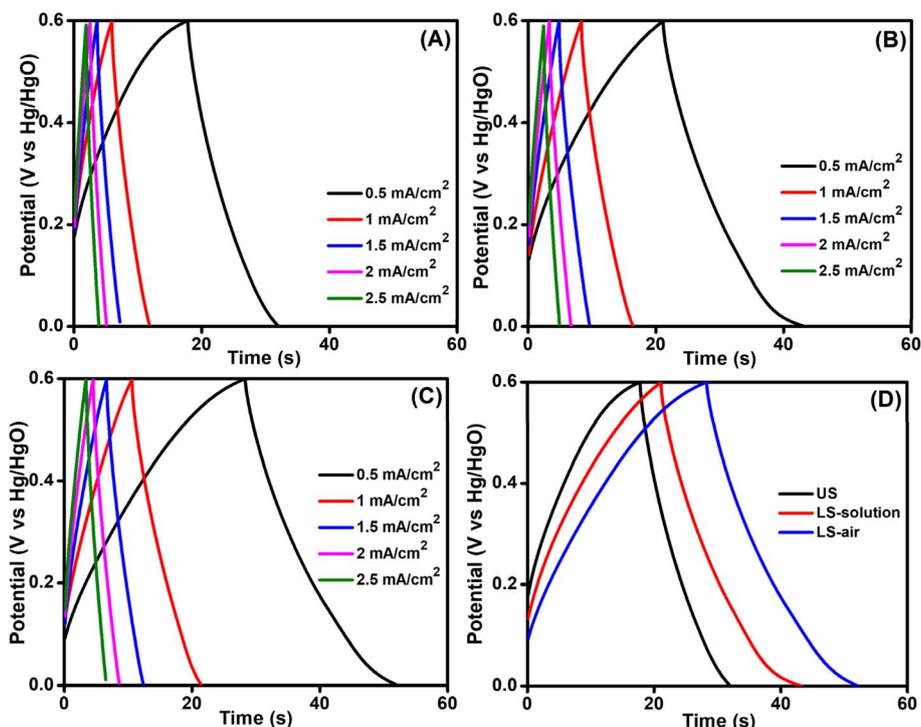| Scan rate (mV s^{-1})	Areal capacitance (mF cm^{-2})			Current density (mA cm^{-2})	Areal-specific capacitance (mF cm^{-2})		
	US	LS-sol.	LS-air		US	LS-sol.	LS-air
5	30.4	35.4	43.6	0.5	11.8	18.5	19.9
10	26.2	33.4	37.4	1.0	9.8	13.5	18.2
20	23.6	29.0	32.9	1.5	9.0	12.0	14.5
40	21.4	25.7	29.7	2.0	8.7	11.3	13.3
60	20.4	23.9	28.0	2.5	8.3	10.4	12.9
80	19.7	22.6	26.9				
100	19.1	21.4	25.8				

Fig. 6 GCD curves of (A) US, (B) LS-solution, (C) LS-air current collectors at different current densities from 0.5 to 2.5 mA cm^{-2} and (D) comparative GCD curves at 0.5 mA cm^{-2} current density for all the samples in 1 M KOH.

electrochemical performance, with longer charge–discharge times in the GCD curves (Fig. 6(B)). As shown in the SEM images, the textured surface created by laser treatment greatly enhanced the electrochemically active area, allowing for efficient ion diffusion and charge storage. The areal-specific capacitance values calculated using GCD curves for this sample were consistently higher than the US sample, particularly at lower current densities, such as 18.5 mF cm^{-2} at 0.5 mA cm^{-2} (Table 1). The LS-air sample exhibited the best electrochemical performance among the prepared samples. A high areal-specific capacitance value of 19.9 mF cm^{-2} at 0.5 mA cm^{-2} was calculated for the LS-air sample (Fig. 6(C)). The GCD curves showed the longest charge–discharge time for the LS-air sample than the US and LS-solution samples at 0.5 mA cm^{-2} (Fig. 6(D)). This significant improvement is attributed to the synergistic effect of laser-induced surface structures and the

superhydrophilic nature of the LS-air sample, which optimized the structural and chemical energy storage properties. Also, the areal-specific capacitance was compared in Fig. S7(b). Overall, the trend reflected the superior energy storage capacity of the LS-air sample, which benefited from a superhydrophilic surface and improved surface area and conductivity. The LS-solution sample offered moderate improvements due to its less pronounced surface structures and lower hydrophilicity. In contrast, the US sample demonstrated the least energy storage capability due to its smooth and passivated surface. The areal-specific capacitance calculated at different current densities is compared in Fig. S7(b) and Table 1. It can be observed from Table 1 that the areal capacitance and areal-specific capacitance decreased with increasing scan rate (in CV) and current density (in GCD). This happens because at a lower scan rate or current density, electrolyte ions have sufficient time to diffuse deeply

into the porous structure and access the full electrochemically active surface area of the electrode. As a result, a larger fraction of the surface contributes to charge storage, yielding higher capacitance values. However, at higher scan rate or current density, the ion diffusion process becomes kinetically limited. Only the outer and more easily accessible surface sites participate in charge storage, while the inner active sites remain underutilized. This limited accessibility, coupled with increased resistive losses at higher current flow, leads to a reduction in the measured capacitance. Therefore, the observed decrease in areal capacitance with increasing scan rate/current density is attributed to the diffusion-controlled insertion.[43–45] Furthermore, the coulombic efficiency of the current collectors was calculated around 84.4% for LS-air, 100% for LS-solution and 81.4% for US sample at 0.5 mA cm^{-2}. Also, the coulombic efficiency for all the current collectors was calculated at different current densities and was found to be above 90% for all the samples at different current densities, which shows the fast and efficient ion diffusion and electron transport processes through the prepared current collectors.

Furthermore, to demonstrate the stability of the prepared current collectors, 5000 GCD cycles were performed at a 1 mA cm^{-2} current density, as depicted in Fig. 7(A). The stability test demonstrated that even after 5000 GCD cycles, the LS-air sample exhibited excellent electrochemical performance since it retained almost 82% efficiency after 5000 GCD cycles compared to the initial capacitance value (Fig. 7(A)). On the other hand, the efficiency was reduced to 77% for the LS-solution and 63% for the US sample. Further, to examine the effect of laser structuring (in air and solution) on the conductivity of the resulting current collectors, all the prepared samples were tested with electrochemical impedance spectroscopy. The Nyquist plot in Fig. 7(B) offered further insights into the impedance characteristics of the prepared current collectors. In Fig. 7(B), the inset shows the equivalent electrical circuit model that we used to fit the Nyquist plots and extract quantitative electrochemical parameters. In the given circuit, R_s represented the resistance of the electrolyte between the working and reference electrodes, while R_{ct} corresponded to the resistance at the electrode–electrolyte interface, related to charge

transfer kinetics. A smaller R_{ct}, in general, indicates better conductivity and faster charge transfer, and C_{dl} models the capacitance formed at the electrode–electrolyte interface due to the electrostatic accumulation of ions (EDLC behavior).[46] The US sample exhibited the highest R_{ct} of 310 Ω, reflecting poor conductivity and slow charge transfer. The LS-solution sample showed a lower R_{ct} value of 184 Ω, highlighting the improved charge transfer capabilities due to laser structuring. The enhanced electrochemical surface area created by the laser treatment and higher Fe content enhanced the ion diffusion and accessibility which resulted in improved conductivity. Similarly, the LS-air sample demonstrated the highest conductivity with the lowest R_{ct} value of 133 Ω. This can be attributed to its grid-like structure with very high electrochemical surface area and superhydrophilic nature which facilitated better charge transfer compared to the US and LS-solution sample.

Our results demonstrate that wastepaper can be effectively transformed into efficient current collectors, offering a low-cost, lightweight, and biodegradable platform for use in flexible supercapacitors. Table 2 presents a comparison between the best-performing current collector developed in this study (LS-air) and other flexible current collectors and electrodes previously reported for supercapacitor applications. The electrochemical performance of LS-air current collector developed in this study was comparable to, and in some cases on par with, previously reported flexible current collectors and electrodes. For example, Ramadoss et al.[47] reported a flexible electrode based on graphene/graphite paper, which exhibited a capacitance of 15.6 mF cm^{-2} at a scan rate of 5 mV s^{-1}. Not only was this capacitance lower than that achieved by the LS-air current collector, but the electrode fabrication procedure also relied on the use of graphene, the synthesis of which is costly via chemical vapor deposition (CVD).[48] Wang et al.[49] used vacuum filtration method to prepare flexible electrode consisting of graphene pillared with carbon black nanoparticles on top of a polyvinylidene fluoride (PVDF) membrane. The reported capacitance was 28 mF cm^{-2} at a scan rate of 10 mV s^{-1}, which remains lower than that of LS-air sample fabricated in this study. Moreover, the mechanical durability of electrodes prepared via vacuum filtration is typically limited since the
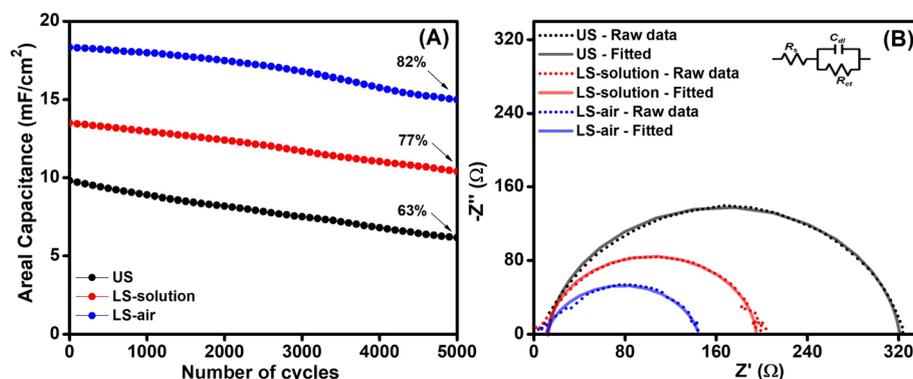

Fig. 7 (A) Capacitance retention at different numbers of cycles and (B) Nyquist plot of the US, LS-solution and LS-air samples recorded in 1 M KOH; (inset) corresponding circuit used to fit EIS data.

Table 2 Comparison of different current collectors/electrodes for flexible supercapacitors

Material	Synthesis details	Electrolyte	Capacitance	Reference
PANI/Au/paper	Paper immersed in polyvinyl alcohol (PVA) solution followed by Au film deposition by e-beam evaporation system and PANI nanowire growth by oxidation of aniline	1 M H_2SO_4	800 mF cm^{-2} at 1 mA cm^{-2}	17
Bacterial cellulose/MWCNTs/PANI paper	Immersion of bacterial cellulose paper into MWCNTs ink followed by coating with PANI for 10 min	1 M H_2SO_4	656 F g^{-1} at 1 A g^{-1}	18
Ni-based filter paper with MnO_2 active material	Treatment of filter paper with $NiCl_2$, H_2PtCl_6, and N_2H_4 followed by dipping for 30 min in $KMnO_4$ solution	1 M Na_2SO_4	1095 mF cm^{-2} at 1 mA cm^{-2}	19
Graphene on flexible graphite-paper	Self-assembly/lift-off technique for depositing graphene (prepared by CVD) on graphite paper	1 M H_2SO_4	15.6 mF cm^{-2} at 5 mV s^{-1}	47
Polyethylenedioxythiophene (PEDOT) paper	Cellulose paper coated with PEDOT (5 coatings) via interfacial polymerization	PVA–H_2SO_4 gel	118 mF cm^{-2}	50
Graphene paper pillared by carbon black nanoparticles	Vacuum filtration of graphene through PVDF membrane in the presence of carbon black nanoparticles	1 M $LiPF_6$	28 mF cm^{-2} at 10 mV s^{-1}	49
Vanadium nitride coated graphite paper	Coating thin films of vanadium nitride on flexible graphite using reactive direct current magnetron sputtering	1 M KOH	91 mF cm^{-2} at 1 mA cm^{-2}	51
Flexible carbon fibers	Treatment with HNO_3	PVA–H_3PO_4 gel	25 mF cm^{-2} at 2 μA cm^{-2}	52
Exfoliated graphite sheet	Thermal exfoliation	3 M KOH	37.08 mF cm^{-2} at 10 mV s^{-1}	
Flexible monofilament fibers	Deposition of AgNPs and Ag nanowires deposition on PVDF fibers by selective laser sintering followed by deposition of thin layers of Gr and MnO_2	PVA–Na_2SO_4	24.5 mF cm^{-2} at 0.1 mA cm^{-2}	53
Vertical graphene/carbon fabric	Growth of vertical graphene on carbon fabric via microwave assisted-plasma enhanced chemical vapor deposition	H_2SO_4 gel polymer	2.4 mF cm^{-2} at 10 mA cm^{-2}	54
Polydopamine/carbon cloth	Dip coating of carbon cloth in dopamine hydrochloride solution	3 M KCl	160.8 mF cm^{-2} at 0.5 mA cm^{-2}	55
Wastepaper	Femtosecond laser structuring in air followed by crosslinking in 50 mM $FeCl_3$ aqueous solution	1 M KOH	43.6 mF cm^{-2} at 5 mV s^{-1}	This work

deposited graphene/carbon black layer does not adhere strongly to the substrate. In contrast, the LS-air current collector exhibits superior mechanical integrity due to the chemical embedding of Fe^{3+} ions within the wastepaper matrix, which contributes to both conductivity and structural robustness. Overall, our results demonstrate that wastepaper can be effectively transformed into flexible current collector for supercapacitor applications through a combination of femtosecond laser structuring and chemical crosslinking with $FeCl_3$ solution. The resulting current collector is low-cost, lightweight, biodegradable, and exhibits excellent electrochemical performance, particularly when laser structuring is conducted in air. Additionally, the fabrication procedure involves reagent-free femtosecond laser processing and the use of a very dilute $FeCl_3$ solution, making the process environmentally friendly and sustainable.

4. Conclusions

We have successfully demonstrated that common wastepaper, an abundant and biodegradable material, can be transformed into a high-performance component, contributing to a cleaner electronic waste stream. Our findings confirm that a two-step process, femtosecond laser structuring in air followed by chemical crosslinking with a dilute $FeCl_3$ solution, yields a current collector with excellent performance. In the first step, wastepaper underwent femtosecond structuring in air or inside a dilute aqueous solution of $FeCl_3$ to generate controlled surface structures that enhanced the electrochemical surface area. Following that, the laser-structured sample was allowed to crosslink in a 50 mM $FeCl_3$ solution for incorporating Fe^{3+} ions into the fibers of the wastepaper. The laser-induced surface modifications in air created a rich, superhydrophilic surface area that significantly improved ion accessibility and charge transfer at the electrode–electrolyte interface. This resulted in a high areal capacitance of 43.6 mF cm^{-2} and robust stability, with 82% capacitance retention after 5000 GCD cycles. These results underscore the critical role of laser processing in unlocking the potential of otherwise inert materials for energy applications. Our primary objective was to address the growing need for sustainable energy storage by developing a low-cost and easily degradable current collector for flexible super-capacitors. For future work, we plan to build upon this success by synthesizing highly active supercapacitor materials and coating them onto these wastepaper-derived current collectors. This next step will aim to fabricate a complete, high-performance electrode, further advancing the development of fully sustainable and efficient flexible energy storage devices.

Author contributions

Muhammad Qasim: writing – original draft, review & editing, visualization, investigation, formal analysis, data curation. Abdul Kareem: writing – original draft, validation, investigation, formal analysis, data curation. Oussama M. El-Kadri: writing – review & editing. Ali Sami Alnaser: writing – review & editing, visualization, validation, supervision, resources, project administration, funding acquisition, conceptualization.

Conflicts of interest

The authors declare that they have no known competing financial interests or personal relationships that could have appeared to influence the work reported in this paper.

Data availability

Data underlying the results presented in this paper are not publicly available at this time but may be obtained from the authors upon reasonable request.

Supplementary information: photographs, EDX patterns, water contact angles, and areal capacitance of the current collectors (word file). Demonstration of superhydrophilicity of LS-air current collector (MP4). See DOI: **https://doi.org/10.1039/d5ra06223c**.

Acknowledgements

References

1 N. Kumar, L. Pradhan and B. K. Jena, *Wiley Interdiscip. Rev. Energy Environ.*, 2022, **11**, e415.

2 N. Maile, S. K. Shinde, S. S. Patil, D.-Y. Kim, A. V Fulari, D. S. Lee and V. J. Fulari, *Ceram. Int.*, 2020, **46**, 14640–14649.

3 B. N. Stram, *Energy Policy*, 2016, **96**, 728–734.

4 A. M. Adeyinka, O. C. Esan, A. O. Ijaola and P. K. Farayibi, *Sustainable Energy Res.*, 2024, **11**, 26.

5 U. V Shembade, S. D. Dhas, S. R. Gurav, S. B. Wategaonkar, S. R. Ghatage, M. A. Gaikwad, V. G. Parale, R. G. Sonkawade, J. H. Kim, H.-H. Park and A. V Moholkar, *Diamond Relat. Mater.*, 2024, **141**, 110602.

6 K. D. Verma, P. Sinha, S. Banerjee and K. K. Kar, in *Handbook of Nanocomposite Supercapacitor Materials I: Characteristics*, ed. K. K. Kar, Springer International Publishing, Cham, 2020, pp. 327–340.

7 Y. Wang, X. Wu, Y. Han and T. Li, *J. Energy Storage*, 2021, **42**, 103053.

8 Q. Xue, J. Sun, Y. Huang, M. Zhu, Z. Pei, H. Li, Y. Wang, N. Li, H. Zhang and C. Zhi, *Small*, 2017, **13**, 1701827.

9 N. A. Salleh, S. Kheawhom and A. A. Mohamad, *Arab. J. Chem.*, 2020, **13**, 6838–6846.

10 A. Abdisattar, M. Yeleuov, C. Daulbayev, K. Askaruly, A. Tolynbekov, A. Taurbekov and N. Prikhodko, *Electrochem. Commun.*, 2022, **142**, 107373.

11 M. Notarianni, J. Liu, F. Mirri, M. Pasquali and N. Motta, *Nanotechnology*, 2014, **25**, 435405.

12 Y. M. Shulga, S. A. Baskakov, E. N. Kabachkov, Y. V Baskakova, N. N. Dremova, O. V Koplak, A. S. Lobach, Y. N. Parkhomenko, V. A. Kazakov, A. R. Tameev and A. Michtchenko, *Langmuir*, 2020, **36**, 8680–8686.

13 L. R. Hepowit, K. M. Kim, S. H. Kim, K. S. Ryu, Y. M. Lee and J. M. Ko, *Polym. Bull.*, 2012, **69**, 873–880.

14 Z. Ren, Y. Li and J. Yu, *iScience*, 2018, **9**, 138–148.

15 M. G. A. Cioffi, D. M. de Oliveira, A. S. C. de Bomfim, K. C. C. de Carvalho Benini, M. O. H. Cioffi and H. J. C. Voorwald, *J. Nat. Fibers*, 2022, **19**, 14089–14101.

16 Y. Ko, M. Kwon, W. K. Bae, B. Lee, S. W. Lee and J. Cho, *Nat. Commun.*, 2017, **8**, 536.

17 L. Yuan, X. Xiao, T. Ding, J. Zhong, X. Zhang, Y. Shen, B. Hu, Y. Huang, J. Zhou and Z. L. Wang, *Angew. Chem., Int. Ed.*, 2012, **51**, 4934–4938.

18 S. Li, D. Huang, B. Zhang, X. Xu, M. Wang, G. Yang and Y. Shen, *Adv. Energy Mater.*, 2014, **4**, 1301655.

19 Y. Li, Q. Wang, Y. Wang, M. Bai, J. Shao, H. Ji, H. Feng, J. Zhang, X. Ma and W. Zhao, *Dalton Trans.*, 2019, **48**, 7659–7665.

20 S. Ghosh, A. Sharma and G. Talukder, *Biol. Trace Elem. Res.*, 1992, **35**, 247–271.

21 R. M. Oshani Nayanathara, W. Leng, S. D. Liyanage, X. Wang, L. Wang, J. Wang, Z. Tian, C. U. Pittman, S. R. Gwaltney and X. Zhang, *Chem. Eng. J.*, 2023, **459**, 141596.

22 C.-C. Wei, P.-H. Lin, C.-E. Hsu, W.-B. Jian, Y.-L. Lin, J.-T. Chen, S. Banerjee, C.-W. Chu, A. P. Khedulkar, R.-A. Doong and K. Tsukagoshi, *Cell Rep. Phys. Sci.*, 2024, **5**, 101836.

23 P. Sathish Kumar, Y. Min, D. C. Hyun, J.-H. Choi and S. Lee, *J. Energy Storage*, 2023, **74**, 109385.

24 M. Guerfali, A. Saidi, A. Gargouri and H. Belghith, *Appl. Biochem. Biotechnol.*, 2015, **175**, 25–42.

25 B. Guo, J. Sun, Y. Hua, N. Zhan, J. Jia and K. Chu, *Nanomanuf. Metrol.*, 2020, **3**, 26–67.

26 J. Yong, Q. Yang, X. Hou and F. Chen, *Ultrafast Sci.*, 2022, DOI: 10.34133/2022/9895418.

27 R. Stoian, A. Rosenfeld, D. Ashkenasi, I. V. Hertel, N. M. Bulgakova and E. E. B. Campbell, *Phys. Rev. Lett.*, 2002, **88**, 097603.

28 S. Lai, Y. Liu, L. Gong, Y. Zhao, C. Zhang and B. Han, *Opt. Laser Technol.*, 2024, **168**, 109871.

29 S. Dittrich, R. Streubel, C. McDonnell, H. P. Huber, S. Barcikowski and B. Gökce, *Appl. Phys. A*, 2019, **125**, 432.

30 H. Hu, T. Liu and H. Zhai, *Opt. Express*, 2015, **23**, 628.

31 H. Liu, F. Chen, X. Wang, Q. Yang, H. Bian, J. Si and X. Hou, *Thin Solid Films*, 2010, **518**, 5188–5194.

32 D. Ołdak, H. Kaczmarek, T. Buffeteau and C. Sourisseau, *J. Mater. Sci.*, 2005, **40**, 4189–4198.

33 S. Y. Oh, D. Il Yoo, Y. Shin and G. Seo, *Carbohydr. Res.*, 2005, **340**, 417–428.

34 M. I. Tanimu, M. A. b. A. Halid, S. K. Loh and R. T. Bachmann, *Biomass Convers. Biorefin.*, 2024, **14**, 27015–27026.

35 S. G. Kostryukov, H. B. Matyakubov, Y. Y. Masterova, A. S. Kozlov, M. K. Pryanichnikova, A. A. Pynenkov and N. A. Khluchina, *J. Anal. Chem.*, 2023, **78**, 718–727.

36 Y. Li, T. Wu, K. Jiang, G. Tong, K. Jin, N. Qian, L. Zhao and T. Lv, *J. Mater. Chem. C*, 2016, **4**, 7119–7129.

37 N. A. Fakhre and B. M. Ibrahim, *J. Hazard. Mater.*, 2018, **343**, 324–331.

38 D. Setyono and S. Valiyaveettil, *J. Hazard. Mater.*, 2016, **302**, 120–128.

39 A. Manna, S. Lahiri, K. Sen and K. Banerjee, *Environ. Monit. Assess.*, 2023, **196**, 54.

40 S. Pasieczna-Patkowska, M. Cichy and J. Flieger, *Molecules*, 2025, **30**, 684.

41 C. Lei, F. Markoulidis, Z. Ashitaka and C. Lekakou, *Electrochim. Acta*, 2013, **92**, 183–187.

42 P. S. Kumar, J. Bae, J. W. Roh, Y. Min and S. Lee, *Nano Convergence*, 2025, **12**, 21.

43 S. Ramar, P. Sathish Kumar, M. Govindaraj, M. K. Muthukumaran, B. K. Raja and A. Selvi, *J. Energy Fuels*, 2025, **39**(21), 10070–10082.

44 G. Kim, I. Ryu and S. Yim, *Sci. Rep.*, 2017, **7**, 8260.

45 W. Yan, T. Ayvazian, J. Kim, Y. Liu, K. C. Donavan, W. Xing, Y. Yang, J. C. Hemminger and R. M. Penner, *ACS Nano*, 2011, **5**, 8275–8287.

46 A. C. Lazanas and M. I. Prodromidis, *ACS Meas. Sci. Au*, 2023, **3**, 162–193.

47 A. Ramadoss, K.-Y. Yoon, M.-J. Kwak, S.-I. Kim, S.-T. Ryu and J.-H. Jang, *J. Power Sources*, 2017, **337**, 159–165.

48 J. Wang, Z. Ren, Y. Hou, X. Yan, P. Liu, H. Zhang, H. Zhang and J. Guo, *N. Carbon Mater.*, 2020, **35**, 193–208.

49 G. Wang, X. Sun, F. Lu, H. Sun, M. Yu, W. Jiang, C. Liu and J. Lian, *Small*, 2012, **8**, 452–459.

50 B. Anothumakkool, R. Soni, S. N. Bhange and S. Kurungot, *Energy Environ. Sci.*, 2015, **8**, 1339–1347.

51 A. Ramadoss, A. Mohanty, K. G. Saravanan, M. Kundu, S. Z. Noby, K. Kirubavathi, K. Selvaraju and L. S. Mende, *Ionics*, 2022, **28**, 2513–2524.

52 J. Lee and G. An, *Appl. Surf. Sci.*, 2021, **539**, 148290.

53 P. T. Nguyen, J. Jang, Y. Lee, S. T. Choi and J. Bin In, *J. Mater. Chem. A*, 2021, **9**, 4841–4850.

54 Z. Yao, B. Quan, T. Yang, J. Li and C. Gu, *Appl. Surf. Sci.*, 2023, **610**, 155535.

55 S. Y. Jung, B. R. Nah, I. W. Cho, J. Choi and M. Yang, *Carbon Lett.*, 2022, **32**, 329–337.